Nanoscale Surface Element Identification and Dopant Homogeneity in the High-T_c Superconductor $\mathrm{Pr}_x\mathrm{Ca}_{1-x}\mathrm{Fe}_2\mathrm{As}_2$

Ilija Zeljkovic,[1] Dennis Huang,[1] Can-Li Song,[1] Bing Lv,[2] Ching-Wu Chu,[2] and Jennifer E Hoffman[1, *]

[1]*Department of Physics, Harvard University, Cambridge, MA 02138, U.S.A.*
[2]*Texas Center for Superconductivity, University of Houston, Houston, TX 77204, U.S.A.*
(Dated: January 22, 2013)

We use scanning tunneling microscopy to determine the surface structure and dopant distribution in $\mathrm{Pr}_x\mathrm{Ca}_{1-x}\mathrm{Fe}_2\mathrm{As}_2$, the highest-$T_c$ member of the 122 family of iron-based superconductors. We identify the cleaved surface termination by mapping the local tunneling barrier height, related to the work function. We image the individual Pr dopants responsible for superconductivity, and show that they do not cluster, but in fact repel each other at short length scales. We therefore suggest that the low volume fraction high-T_c superconducting phase is unlikely to originate from Pr inhomogeneity.

The recent discovery of high-T_c superconductivity in Fe-based materials[1] has rejuvenated worldwide efforts to understand and predict new superconductors. Fe-based superconductors (Fe-SCs) share several characteristics with their cuprate cousins. First, their chemical structure consists of Fe-based superconducting planes separated by buffer layers. Second, superconductivity usually arises by electron or hole doping a stoichiometric antiferromagnetic parent compound[2]. Third, Fe-SCs show nanoscale electronic inhomogeneity[3, 4], necessitating the use of local tools for complete understanding.

The first generation of the $A\mathrm{Fe}_2\mathrm{As}_2$ (122) family of Fe-SCs seemed similar to cuprates, because hole doping this family resulted in a much higher maximum T_c (38 K in $\mathrm{K}_x\mathrm{Ba}_{1-x}\mathrm{Fe}_2\mathrm{As}_2$ [5]) than electron doping (25 K in $\mathrm{Ba}(\mathrm{Fe}_{1-x}\mathrm{Co}_x)_2\mathrm{As}_2$ [6]). It was pointed out that the highest T_c of all Fe-SCs arose in an electron-doped member of a different structural family (57 K in $\mathrm{Sm}_{1-x}\mathrm{La}_x\mathrm{O}_{1-y}\mathrm{F}_y\mathrm{FeAs}$ [7]). This suggested that the T_c in electron-doped $A(\mathrm{Fe}_{1-x}\mathrm{Co}_x)_2\mathrm{As}_2$ might be artificially suppressed by the Co dopants, which play a dual role of providing the charge carriers necessary for superconductivity, but also introducing damaging disorder directly into the crucial Fe layer. It was hypothesized that electron doping into the buffer layer between the crucial Fe layers could provide the charge carriers without the disorder, and perhaps allow a higher T_c in the electron-doped 122 materials. Indeed, this was found to be the case in the rare-earth-doped Ca122 family[8, 9], with T_c reaching 49 K in $\mathrm{Pr}_x\mathrm{Ca}_{1-x}\mathrm{Fe}_2\mathrm{As}_2$. However, the high T_c appeared in only $\sim 10\%$ of the volume, while the bulk of the material showed $T_c \sim 10 - 20$ K.

Saha *et al.* performed a thorough search for the origin of the low volume fraction high-T_c phase, using bulk experimental probes. First, the high T_c was found to be impervious to etching or oxidation, arguing against surface superconductivity. Second, high-T_c resistive transitions were never observed for dopant concentrations below those necessary to suppress the parent antiferromagnetic phase, arguing against any randomly occurring

impurities or contaminant phases as the origin. Furthermore, no such contaminant phases were observed in over 20 samples examined by x-ray diffraction. Third, the high T_c was unaffected by the global structural collapse phase transition (the abrupt $\sim 10\%$ shrinkage of the c-axis lattice constant that occurs in the Ca122 family under external or chemical pressure), arguing against any relationship to the collapsed phase or to interfaces between collapsed and non-collapsed phases. Finally, it was noted that aliovalently-doped $\mathrm{CaFe}_2(\mathrm{As}_{1-x}\mathrm{P}_x)_2$ also shows the structural collapse but no high-T_c volume fraction [10]. Saha *et al.* therefore concluded that the charge doping is an essential ingredient to the high-T_c phase, and speculated on the low volume fraction high-T_c phase "as having a localized nature tied to the low percentage of rare earth substitution."

Given the challenges in identifying the origin of the low volume fraction high-T_c phase from bulk experiments, a local probe is naturally required. Here we use scanning tunneling microscopy (STM) to investigate two possible sources of electronic inhomogeneity in $\mathrm{Pr}_x\mathrm{Ca}_{1-x}\mathrm{Fe}_2\mathrm{As}_2$: the surface and the dopants. We provide the first definitive identification of the cleaved surface termination and the first image of all individual dopants in the Ca122 system. Our results suggest that dopant inhomogeneity is unlikely to be responsible for the low volume fraction of high-T_c superconductivity in $\mathrm{Pr}_x\mathrm{Ca}_{1-x}\mathrm{Fe}_2\mathrm{As}_2$.

Single crystals of $\mathrm{Pr}_x\mathrm{Ca}_{1-x}\mathrm{Fe}_2\mathrm{As}_2$ are grown via self-flux with measured $x = 10.5\%$ and resistive $T_c = 43.2$ K. The crystals are handled exclusively in Ar environment, cleaved in ultra-high vacuum at cryogenic temperature, and immediately inserted into the STM head where they are imaged with a mechanically sharpened PtIr tip, cleaned by field emission on Au. The first challenge in STM imaging of any new material is to identify the surface structure and evaluate to what extent it is representative of the bulk. The surface structure of the $A\mathrm{Fe}_2\mathrm{As}_2$ system has been particularly controversial [11]. Due to the stronger bonding within the FeAs layer [Fig. 1(a)], the FeAs layer is expected to remain intact, leaving half
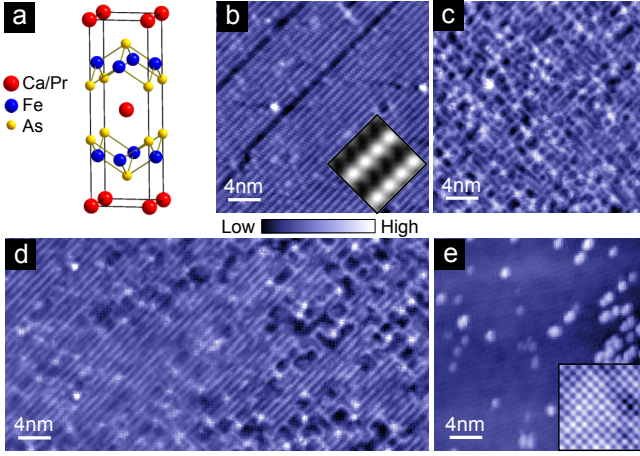
FIG. 1. (color online) Surface morphologies of cold-cleaved $Pr_{0.105}Ca_{0.895}Fe_2As_2$. (a) Crystal structure of $Pr_xCa_{1-x}Fe_2As_2$. Topographs of (b) 2×1 surface structure (250 pA, +300 mV, 7 K) (c) disordered, "web-like" surface structure (15 pA, 100 mV, 7 K), (d) smooth transition between 2×1 and "web-like" structures (20pA, -100mV, 7K), and (e) 1×1 square lattice with ~ 4 Å lattice constant (5 pA, 50 mV, 25 K). Inset in (b) shows an average 30×15 pixel, 2×1 supercell [17] tiled 2×4 times. Inset in (e) shows an enlarged, 4 nm topograph of 1×1 square lattice acquired at 50 mV and 50 pA. (Due to an external noise source present during the acquisition of the data in panel (e), the images in (e) have been filtered to remove all spurious spatial frequencies higher than the 4 Å periodicity.)

TABLE I. Work functions for several elements[18].

Atom	Fe	As	Ca	Pr	Sr	Ba	Au	Pt	Ir
φ (eV)	4.65	3.75	2.71	2.7	2.76	2.35	5.32	5.40	5.6

a complete A layer on each surface [12]. This preservation of charge neutrality is a necessary (but not sufficient) condition for the surface to be representative of the bulk. However, a number of experiments have claimed that the cleaved surface is As-terminated in the Ba122 [13], Sr122 [14], and Ca122 [15] systems.

We encounter three different surface morphologies in our STM topographs of $Pr_{0.105}Ca_{0.895}Fe_2As_2$. The majority of the observed sample surface displays a 2×1 structure [Fig. 1(b)] frequently observed in other STM studies of 122 materials [16]. We occasionally observe a disordered, "web-like" structure [Fig. 1(c)], which smoothly merges with the 2×1 structure [Fig. 1(d)]. The third type of surface, observed rarely, shows a 1×1 square lattice with ~ 4 Å periodicity [Fig. 1(e)].

We map the tunneling barrier height to identify these surfaces. The tunneling current I is expected to decay exponentially with the tip-sample separation z as

$$I \propto e^{-\sqrt{\frac{8m_e\Phi}{\hbar^2}}z} \qquad (1)$$

where Φ is the local barrier height (LBH), approximately equal to the average of the tip and sample work functions [19]. Due to the large variation in the work functions of the elemental components of 122 Fe-SCs (Table I), a simple measurement of the LBH should in principle be sufficient to determine the surface termination. However, the LBH is sensitive not only to the elemental composition of the tip, but also the geometric configuration of the tip's terminal atoms, and the tip-sample angle (which reduces the LBH by $\cos^2\theta$, where θ is the deviation between the sample surface perpendicular and the z direction of tip piezo motion [20]). Moreover, the LBH depends on the sample topography through two opposing mechanisms. On the one hand, protruding atoms or clusters may deform easily, stretching out as the tip is retracted, decreasing the effective rate at which the tip-sample distance decreases, and thus suppressing the measured LBH above the protrusion [21]. On the other hand, the topographic corrugation appears smoothed out at distances far from the surface; this implies that the wave function must decay faster above a protrusion than a depression, thus enhancing the measured LBH above a protrusion [22]. Without accounting for these factors, previous studies found the LBH on the 2×1 surface of $BaFe_2As_2$ to be much lower than the expected work functions for either Ba or As [23].

In contrast, the comparison of LBH measurements with the same tip (i.e. the same microscopic configuration of terminating atoms) across different flat regions of the same cleaved surface (i.e. the same tip-sample angle) can yield a robust measure of relative work functions, and can be utilized for element identification in cases where the sample consists of two different surfaces [24]. Here, we directly compare LBH values measured with the same STM tip across the different morphologies of Fig. 1 on the same cleaved sample.

In order to extract the LBH, at each point (x, y) in a field of view (FOV) a feedback loop adjusts $z_0(x, y)$ to maintain $I = 100$ pA at $V_{set} = -100$ mV; the feedback loop is then discontinued and the current $I(z)$ is measured as the tip is retracted continuously from z_0. Figure 2 shows simultaneous topographs and work function maps for the 1×1 square lattice across a step edge [Figs. 2(a,c)] and the 2×1 structure in a nearby flat area [Figs. 2(b,d)]. Figure 2(e) shows two sets of representative $I(z)$ curves from the square regions in Figs. 2(a,b). Despite the small spread within each set of $I(z)$ curves, the two sets are clearly distinct from one another. After correcting for the surface slope, we find the average LBH values are $\Phi_{1\times1} = 4.50 \pm 0.42$ eV and $\Phi_{2\times1} = 3.57 \pm 0.34$ eV. In comparison with Table I, and after taking the tip work function into account, these values suggest that the 1×1 surface is a complete As layer, while the 2×1 surface is a half Ca layer.

To quantify this identification, we note that charge redistribution at a surface may give rise to an additional

dipole barrier, which can increase or decrease the measured LBH according to the dipole orientation [25]. We would therefore expect

$$\Phi_{1\times 1} = \frac{\varphi_{As} + E_{d,As} + \varphi_{tip}}{2}; \quad \Phi_{2\times 1} = \frac{\varphi_{Ca} + E_{d,Ca} + \varphi_{tip}}{2} \tag{2}$$

where φ_{As} and φ_{Ca} are the element work functions, and $E_{d,As}$ and $E_{d,Ca}$ are the additional energies for an electron to escape the dipole layers at the As- and Ca-terminated surfaces. Assuming $\varphi_{tip} \lesssim \varphi_{PtIr}$ [26], Eq. (2) yields values of $E_{d,As}$, $E_{d,Ca}$, and their difference $E_{d,As} - E_{d,Ca} = 0.82$ eV that are all of the correct magnitude for such dipole layers[25]. The sign of the difference, which indicates that it is harder to remove an electron from the dipole barrier of the As surface than that of the half-Ca surface, is physically justified because the half-Ca surface is nonpolar, whereas the As surface is deficient of electrons from the stripped Ca, and thus more electronegative. The inferred electron-deficiency of this As surface is consistent with the failure to observe even proximity-induced superconductivity on the As-terminated surface of the related $Sr_{0.75}K_{0.25}Fe_2As_2$ [27].

We also note the reduced LBH along the step edge in Fig. 2(c). Such LBH reduction at step edges has been seen in other systems, and may be attributed to a combination of two mechanisms [24]. First, the step edge is effectively an angled surface, so the LBH is reduced by $\cos^2 \theta$. Second, the Smoluchowski smoothing of the electron wave functions along the step edge results in an additional dipole moment which reduces the LBH [28].

To further support the identification of the 2×1 surface, we show a high-resolution map of the intra-unit cell structure to rule out the possibility of "hidden" surface atoms. We correct for small piezoelectric and thermal drift by placing the Ca/Pr atoms of Fig. 1(b) on a perfect lattice [29]. We then use the whole FOV to create the high-resolution average 2×1 supercell in the inset to Fig. 1(b) [17]. We do not observe atom dimerization (as seen in $Ca_{0.83}La_{0.17}Fe_2As_2$ [15] and $Sr_{1-x}K_xFe_2As_2$ [14, 30]), but rather a single row of atoms, similar to the $CaFe_2As_2$ parent compound [31].

For completeness, we investigate the nature of the "web-like" surface. Because it merges smoothly into the 2×1 surface without any sharp transitions that could be attributed to step edges [Fig. 1(d)], the "web-like" surface is also likely a reconstruction of the Ca layer. Simultaneous topograph and LBH map of the "web-like" surface are shown in Figs. 3(a,c), with analogous maps for the 2×1 surface, acquired with the same tip for direct comparison, shown in Figs. 3(b,d). Bright spots in the topograph of Fig. 3(a) exhibit much higher LBH than surrounding areas. Anomalously high LBH at these atomic-scale features reinforces the importance of the geometric effects of protrusions on the measured LBH, and the necessity of flat atomic planes in order to extract a reliable
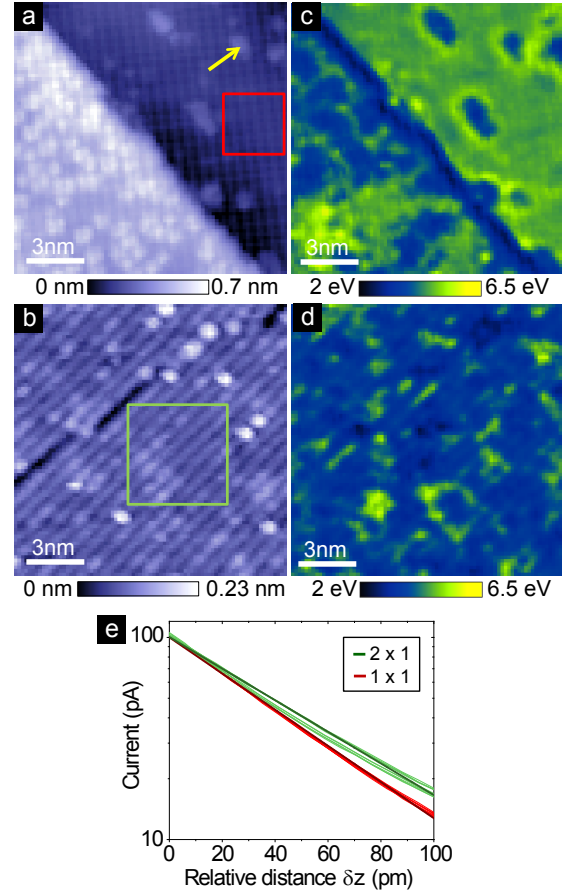

FIG. 2. (color online) LBH comparison between 1×1 and 2×1 surface structures. Topographs acquired at 25 K of (a) 1×1 (4 Å × 4 Å) square lattice appearing on both sides of a step edge and (b) 2×1 (8 Å × 4 Å) lattice. Simultaneously acquired LBH maps are shown in (c) and (d). Approximately 26% larger LBH is observed in a clean, flat area of the 1×1 surface (red box in (a)) than in a clean flat area of the 2×1 surface (green box in (b)). Furthermore, sparse topographic protrusions on the 1×1 surface (e.g. marked by yellow arrow) show a lower LBH close to that of the flat 2×1 surface, suggesting that they are scattered remaining Ca or Pr atoms. Both datasets were acquired at I_{set}=100 pA and V_{set}=-100 mV. (e) Representative sets of $I(z)$ curves from square regions in (a) and (b) are shown as thin red and green lines respectively. Darker red and green lines represent linear fits to the average $I(z)$ curves from boxes in (a) and (b).

LBH comparison. Further conclusions from Fig. 3 would require a quantitative understanding of these geometric protrusion effects. We reiterate that our identification of the 1×1 surface as a complete As layer and the 2×1 surface as a half-Ca layer is robustly drawn from the flat surfaces in Fig. 2.

Since φ_{Ca} and φ_{Pr} differ by less than 1% (Table I), LBH mapping cannot be used to identify Pr atoms in the Ca surface layer. However, STM can image dopants as atomic-scale features in the differential conductance
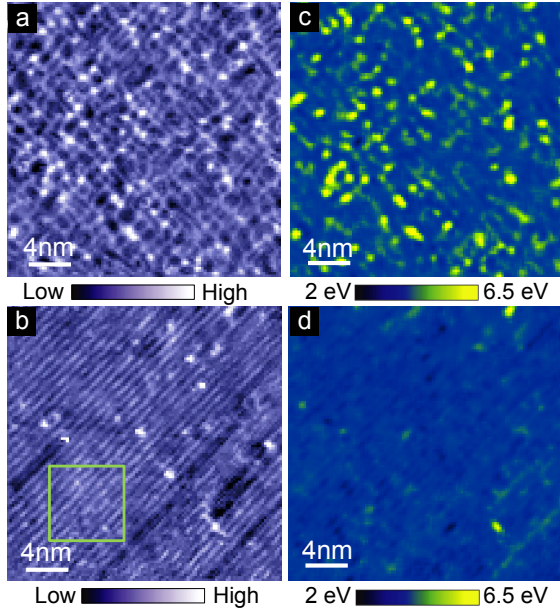
FIG. 3. (color online) LBH comparison between "web-like" and 2×1 surface structures. Topographs acquired at 7 K of (a) "web-like" surface and (b) 2×1 surface. Simultaneously acquired LBH maps are shown in (c) and (d). Anomalously high LBH values are measured over the bright, atomic-scale features in (a). Both datasets were acquired at I_{set}=105 pA and V_{set}=-100 mV. The z calibration used here was obtained by assuming that the average LBH for the 2×1 surface in the boxed region of (b) here is the same as that in Fig. 2(d).

FIG. 4. (color online) Map of Pr dopants. (a) dI/dV image at +300 mV showing Pr dopants as bright atomic-scale features from the same FOV as Fig. 1(b). (b) Radial distribution ratios for two sets of Pr dopants. Full squares represent the distribution of Pr dopants shown in (a), while open squares represent a different dataset used to confirm the conclusions. Inset shows a 2.5 nm × 2.5 nm region in which surface Ca positions (white dots) and Pr dopants (yellow dots) have been marked, demonstrating our ability to resolve individual Pr dopants even at adjacent Ca sites.

dI/dV, which is proportional to the local density of states [32]. Substituting Pr^{3+} for Ca^{2+} creates a localized positive charge, so the impurity state is expected above the Fermi level. We therefore search for Pr dopants in dI/dV images at high bias. Figure 4(a) shows a dI/dV image obtained simultaneously with the topograph in Fig. 1(b) at +300 mV, revealing a set of bright, atomic-scale features. These features, which start to appear in dI/dV at biases higher than +70 mV, comprise ~10.4% of the total number of visible atoms in this FOV [33], matching the macroscopically measured $x = 10.5\%$. The appearance of the expected concentration of Pr^{3+} dopants on the surface confirms the half-Ca termination. Although a subset of Co dopants were previously imaged in $Ca(Fe_{1-x}Co_x)_2As_2$ [31], this is the first time that *all* dopants have been imaged in a Ca122 system.

Because we have imaged *all* dopants, we can investigate the possibility of clustering, which was suggested as the origin of the inhomogeneous high-T_c phase [8]. We compute a "radial distribution ratio" (RDR) by histogramming all observed Pr-Pr distances within a FOV, then dividing this observed histogram by an average histogram of 1000 simulated random dopant distributions at the same concentration. The RDR in Fig. 4(b) shows no clustering, and in fact slight repulsion of the Pr dopants
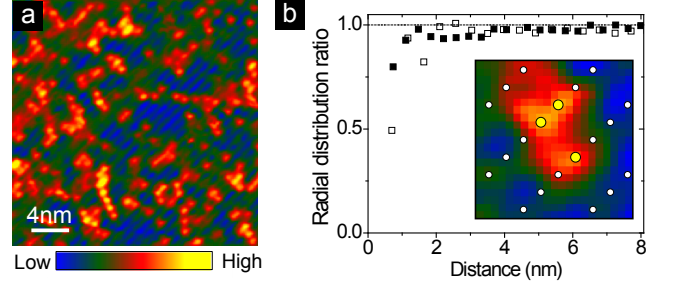
at short distances, possibly due to their like charges. The repulsion is not an artifact of poor dopant identification, as illustrated by clear detection of two adjacent Pr dopants in the inset to Fig. 4(b). The lack of dopant clustering in $Pr_xCa_{1-x}Fe_2As_2$ contrasts with the Se dopants in $FeTe_{1-x}Se_x$ that are prone to forming patches of ~1 nm size [34]. This contrast may arise from the ~10% size mismatch of Se (198 pm) and Te (221 pm) vs. the similar sizes of Ca (126 pm) and Pr (126.6 pm) [27, 35]. Our observation of the expected number of Pr dopants, more homogeneously distributed than would be expected for a random distribution, suggests that dopant clustering is unlikely to be responsible for the small volume fraction high-T_c superconducting state.

In conclusion, our STM images of the highest-T_c member of the 122 family, $Pr_xCa_{1-x}Fe_2As_2$, have addressed its surface structure and dopant distribution, with bearing on the high-T_c volume fraction. First, we used LBH mapping to identify the 2×1 surface as a half-Ca termination, and the 1×1 surface as an As termination. This LBH mapping method could be used to resolve debated cleaved surface terminations in a wide variety of materials, such as other Fe-SCs [36] or a number of heavy fermion materials which have recently been cleaved and imaged by STM for the first time [37, 38]. Second, we imaged the Pr dopants responsible for superconductivity, the first time that all dopants have been identified in Ca122. We demonstrated that Pr dopants do not cluster, and in fact show a slight tendency to repel each other at very short length scales. Our findings suggest that Pr inhomogeneity is unlikely to be the source of the high-T_c volume fraction, in contrast to previous speculation [8].

----

* jhoffman@physics.harvard.edu

[1] Y. Kamihara, T. Watanabe, M. Hirano, and H. Hosono, J. Am. Chem. Soc. **130**, 3296 (2008).

[2] D. C. Johnston, Adv. Phys. **59**, 803 (2010).

[3] Y. Yin, M. Zech, T. L. Williams, X. F. Wang, G. Wu, X. H. Chen, and J. E. Hoffman, Phys. Rev. Lett. **102**, 97002 (2009).

[4] F. Massee, Y. Huang, R. Huisman, S. De Jong, J. B. Goedkoop, and M. S. Golden, Phys. Rev. B **79**, 220517 (2009).

[5] M. Rotter, M. Tegel, and D. Johrendt, Phys. Rev. Lett. **101**, 107006 (2008).

[6] Y. Nakajima, T. Taen, and T. Tamegai, J. Phys. Soc. Jap. **78**, 023702 (2009).

[7] Z. Wei, H. Li, W. L. Hong, Z. Lv, H. Wu, X. Guo, and K. Ruan, Journ. of Supercond. and Nov. Mag. **21**, 213 (2008).

[8] S. R. Saha, N. P. Butch, T. Drye, J. Magill, S. Ziemak, K. Kirshenbaum, P. Y. Zavalij, J. W. Lynn, and J. Paglione, Phys. Rev. B **85**, 024525 (2012).

[9] B. Lv, L. Deng, M. Gooch, F. Wei, Y. Sun, J. K. Meen, Y. Y. Xue, B. Lorenz, and C. W. Chu, Proc. Nat. Acad. Sci. **108**, 15705 (2011).

[10] S. Kasahara, T. Shibauchi, K. Hashimoto, Y. Nakai, H. Ikeda, T. Terashima, and Y. Matsuda, Phys. Rev. B **83**, 060505 (2011).

[11] J. E. Hoffman, Rep. Prog. Phys. **74**, 124513 (2011).

[12] M. Gao, F. Ma, Z. Y. Lu, and T. Xiang, Phys. Rev. B **81**, 193409 (2010).

[13] V. B. Nascimento, A. Li, D. R. Jayasundara, Y. Xuan, J. O'Neal, S. Pan, T. Y. Chien, B. Hu, X. B. He, G. Li, A. S. Sefat, M. A. McGuire, B. C. Sales, D. Mandrus, M. H. Pan, J. Zhang, R. Jin, and E. W. Plummer, Phys. Rev. Lett. **103**, 076104 (2009).

[14] F. C. Niestemski, V. B. Nascimento, B. Hu, W. Plummer, J. Gillett, S. E. Sebastian, Z. Wang, and V. Madhavan, arXiv **0906.2761** (2009), arXiv:0906.2761.

[15] Y. B. Huang, P. Richard, J. H. Wang, X. P. Wang, X. Shi, N. Xu, Z. Wu, A. Li, J. X. Yin, T. Qian, B. Lv, C. W. Chu, S. H. Pan, M. Shi, and H. Ding, arXiv **1210.7288** (2012), arXiv:1210.7288.

[16] F. Massee, S. de Jong, Y. Huang, J. Kaas, E. van Heumen, J. B. Goedkoop, and M. S. Golden, Phys. Rev. B **80**, 140507 (2009).

[17] I. Zeljkovic, E. J. Main, T. L. Williams, M. C. Boyer, K. Chatterjee, W. D. Wise, Y. Yin, M. Zech, A. Pivonka, T. Kondo, T. Takeuchi, H. Ikuta, J. Wen, Z. Xu, G. D. Gu, E. W. Hudson, and J. E. Hoffman, Nat. Mat. **11**, 585 (2012).

[18] J. Speight, *Lange's Handbook of Chemistry*, 16th ed. (McGraw-Hill, 2005) p. 1.132.

[19] G. Binnig, N. Garcia, H. Rohrer, J. Soler, and F. Flores, Phys. Rev. B **30**, 4816 (1984).

[20] R. Wiesendanger, L. Eng, H. R. Hidber, P. Oelhafen, L. Rosenthaler, U. Staufer, and H. J. Guntherodt, Surf. Sci. **189-190** (1987), 10.1016/S0039-6028(87)80410-7.

[21] Y. Yamada, A. Sinsarp, M. Sasaki, and S. Yamamoto, Jap. J. App. Phys. **42**, 4898 (2003).

[22] R. Wiesendanger, *Scanning probe microscopy and spectroscopy* (Cambridge University Press, 1994) Chap. 1.12.

[23] F. Massee, *A tunneler's view on correlated oxides and iron based superconductors*, Ph.D. thesis, University of Amsterdam, Amsterdam, The Netherlands (2011).

[24] J. F. Jia, K. Inoue, Y. Hasegawa, W. S. Yang, and T. Sakurai, Phys. Rev. B **58**, 1193 (1998).

[25] E. Wigner and J. Bardeen, Phys. Rev. **48**, 84 (1935).

[26] Our LBH measurements using PtIr tips on Au samples typically yield effective φ_{tip} somewhat less than the elemental work functions of the constituants. This observation is also typical in the literature, e.g. in Ref. 21.

[27] C.-L. Song, Y. Yin, M. Zech, T. Williams, M. Yee, G.-F. Chen, J.-L. Luo, N.-L. Wang, E. W. Hudson, and J. E. Hoffman, arXiv **1212.3240** (2012), arXiv:1212.3240.

[28] R. Smoluchowski, Phys. Rev. **60**, 661 (1941).

[29] M. J. Lawler, K. Fujita, J. Lee, A. R. Schmidt, Y. Kohsaka, C. K. Kim, H. Eisaki, S. Uchida, J. C. Davis, J. P. Sethna, and E. A. Kim, Nature **466**, 347 (2010).

[30] M. C. Boyer, K. Chatterjee, W. D. Wise, G. F. Chen, J. L. Luo, N. L. Wang, and E. W. Hudson, arXiv **0806.4400** (2008), arXiv:0806.4400.

[31] T. M. Chuang, M. P. Allan, J. Lee, Y. Xie, N. Ni, S. L. Budko, G. S. Boebinger, P. C. Canfield, and J. C. Davis, Science **327**, 181 (2010).

[32] I. Zeljkovic, Z. Xu, J. Wen, G. Gu, R. S. Markiewicz, and J. E. Hoffman, Science **337**, 320 (2012).

[33] The dopant locator algorithm consists of four user-tunable parameters: neighborhood size (NS), duplicate distance (DD), smoothing window (SW), and local threshold (LT). For each pixel (x, y) in the FOV, the algorithm finds the position of the local maximum (LM) within a square of side NS centered at (x, y). From the set of LMs (x_i, y_i), the algorithm eliminates those within DD of a brighter LM, and those whose relative brightness compared to the regional average, defined as the average value within a square of side $2\mathrm{SW} + 1$ centered at (x_i, y_i), is less than LT. To identify the dopants in Fig. 3a, we used DD=2.4 Å(*cf.* Ca-Ca nearest-neighbor distance 4 Å), NS=4.8 Å, and SW=109 Å. Qualitative conclusions about the absence of clustering and short lengthscale repulsion of Pr dopants were unaffected by up to 28% variation of SW and 15% variation of LT.

[34] X. He, G. Li, J. Zhang, A. Karki, R. Jin, B. Sales, A. Sefat, M. McGuire, D. Mandrus, and E. Plummer, Phys. Rev. B **83**, 220502 (2011).

[35] R. D. Shannon, Act. Cryst. Sec. A **32**, 751 (1976).

[36] S. Grothe, S. Chi, P. Dosanjh, R. Liang, W. Hardy, S. Burke, D. Bonn, and Y. Pennec, Phys. Rev. B **86**, 174503 (2012).

[37] A. R. Schmidt, M. H. Hamidian, P. Wahl, F. Meier, a. V. Balatsky, J. D. Garrett, T. J. Williams, G. M. Luke, and J. C. Davis, Nature **465**, 570 (2010).

[38] P. Aynajian, E. H. da Silva Neto, A. Gyenis, R. E. Baumbach, J. D. Thompson, Z. Fisk, E. D. Bauer, and A. Yazdani, Nature **486**, 201 (2012).